International Journal of Computational and Experimental Science and ENgineering (IJCESEN)

Vol. 12-No.1 (2026) pp. 1485-1495
http://dergipark.org.tr/en/pub/ijcesen

ISSN: 2149-9144

Research Article

Comparative Analysis of Secondary Particle Production and Spatial Dose Distributions in Multilayer Concrete-Iron Shielding Systems for a 50 MeV Proton Accelerator Using FLUKA

Demet Sariyer[1]*, Mustafa Emre Erbil[2]

[1]Manisa Celal Bayar University, Turgutlu Vocational High School, Turgutlu, Manisa, Turkey
* **Corresponding Author Email:** demet.sariyer@cbu.edu.tr **ORCID:** 0000-0002-7803-111X

[2]Manisa Celal Bayar University, Hasan Ferdi Turgutlu Faculty of Technology, Turgutlu, Manisa, Turkey
Email: 2540098004@ogr.cbu.edu.tr - **ORCID:** 0009-0003-9394-8588

Article Info:

DOI: 10.22399/ijcesen.5083
Received : 05 February 2026
Revised : 22 March 2026
Accepted : 25 March 2016

Keywords

Proton accelerators,
Monte Carlo simulation,
FLUKA,
neutron shielding,
Multilayer shielding,
Iron-concrete shielding

Abstract:

Proton accelerators operating in the medium-energy range generate complex secondary radiation fields due to proton-target interactions, where neutrons constitute the dominant component from a shielding perspective. In such systems, the design of effective shielding structures requires not only appropriate material selection but also optimized layer arrangement and geometry. Although multilayer shielding approaches have been widely studied, systematic comparisons of iron–concrete configurations with varying layer sequences and structural complexity remain limited.In this study, secondary particle production and spatial dose distributions generated by 50 MeV protons interacting with a copper target were investigated under two different multilayer shielding configurations composed of iron and concrete. The first configuration consists of a complex hybrid structure with multiple iron layers embedded within concrete, while the second employs a simplified arrangement with a single inner iron layer surrounded by concrete. Monte Carlo simulations were performed using the FLUKA code to evaluate secondary particle yields and two-dimensional dose distribution maps in terms of ambient dose equivalent H*(10). The results indicate that total secondary particle production and relative particle contributions remain nearly identical for both shielding designs, confirming that particle generation is primarily governed by proton–target interactions. However, significant differences were observed in spatial dose distributions. The multilayer hybrid configuration leads to more heterogeneous and spatially extended dose fields due to increased scattering and material interface effects, whereas the simplified configuration provides a more confined and homogeneous radiation field with sharper attenuation characteristics. These findings demonstrate that shielding performance is strongly influenced by layer arrangement and geometric complexity rather than particle production alone. The study highlights the importance of spatial dose control in multilayer shielding design and provides new insights into the optimization of iron–concrete hybrid shielding systems for medium-energy proton accelerator applications.

1. Introduction

Proton accelerators are widely used in a broad range of applications, from medical treatments to nuclear physics research and industrial processes, and systems operating in the medium-energy range (10-100 MeV) are particularly critical in terms of secondary radiation production and shielding requirements [1]. In such systems, secondary particles generated as a result of proton interactions with target and surrounding materials lead to highly heterogeneous and non-linear spatial dose distributions [2,3]. Although various particle types contribute to this secondary radiation field, neutrons are known to be the dominant component from a shielding perspective, especially in the 50 MeV energy regime [3,4]. Due to their electrically neutral nature, high penetration capability, and ability to transport across a wide energy spectrum, neutrons constitute one of the primary factors governing shielding design [5,6].Since neutrons are electrically neutral, they do not produce direct ionization, and

their energy loss occurs mainly through nuclear interaction processes [7,8]. These interactions include elastic and inelastic scattering, nuclear reactions, and secondary particle production mechanisms [8,9]. The strong energy dependence of neutron interaction cross-sections results in significant variations in moderation, scattering, and absorption processes across different materials [9,10]. This leads to the inadequacy of single-material shielding solutions in many cases and necessitates the use of multilayer shielding configurations [10,11].Considering neutron energies around 50 MeV, material selection and arrangement in multilayer shielding systems must be optimized in accordance with energy-dependent interaction mechanisms [7,12]. In this energy range, neutron–nucleus interactions remain significant, and inelastic scattering processes play an important role in reducing neutron energy [7,9]. In this context, high-density iron layers are effective in the initial attenuation stage by transferring neutron energy to lower levels through inelastic scattering and nuclear excitation processes [9,14]. The moderated neutrons are then further slowed down in subsequent concrete layers, where hydrogen content and intermediate atomic number elements enhance elastic scattering processes, leading to efficient energy reduction toward thermal ranges [8,15]. This moderation process increases the probability of neutron absorption at lower energies, thereby improving shielding effectiveness [10]. The surrounding soil medium provides additional attenuation through both further moderation and absorption mechanisms, particularly for low-energy neutrons, depending on its composition and moisture content [10,11]. Therefore, multilayer shielding configurations consisting of sequential iron, concrete, and soil layers provide a physically consistent and effective engineering solution for the gradual energy degradation of neutrons with an initial energy of 50 MeV and for the reduction of environmental dose levels [11,12].A large number of experimental and numerical studies on accelerator shielding and secondary particle production have been reported in the literature. Secondary particle production and transport in medium-energy proton-matter interactions have been extensively investigated. The FLUKA code developed by Ferrari et al. (2005) enables reliable calculation of proton-induced secondary particle production by accurately modeling hadronic and electromagnetic interactions over a wide energy range [13]. Similarly, MCNP-based studies developed by Pelowitz et al. (2011) have demonstrated the accuracy of Monte Carlo (MC) methods, particularly in neutron transport and dose calculations [16]. The GEANT4 simulation framework developed by Agostinelli et al. (2003) has also been widely used to investigate the effects of different material configurations on secondary particle spectra [17].Sullivan (1992) examined radiation fields around high-energy accelerators and demonstrated the critical role of neutrons in shielding [18]. Liu et al. (1993) analyzed neutron fields in proton accelerators in detail and showed that neutrons provide the largest contribution to total dose equivalent [19]. Studies on the energy and angular distributions of neutrons produced from proton–nucleus interactions were conducted by Agosteo et al. (2007), highlighting the dominant role of high-energy neutrons [20].With the development of MC methods, accelerator shielding problems have been investigated in a more detailed and reliable manner. Studies by Pelliccioni (2000) on operational dose quantities have made significant contributions, particularly in determining fluence-to-dose conversion coefficients for neutron fields [21]. Sarıyer and Küçer (2013) analytically investigated required shielding thicknesses for different materials in proton accelerators and demonstrated the dominant role of neutrons [22].Recent studies have focused on the neutron attenuation performance of different shielding materials and multilayer structures. MC simulations have shown that multilayer shielding systems combining concrete, iron, and boron-containing materials provide higher efficiency in neutron moderation and absorption [23,24]. In subsequent studies (Sarıyer and Küçer, 2014), the performance of concrete and soil shielding systems in the 100–250 MeV energy range was evaluated using MC simulations [25]. Further investigations determined the required shielding thicknesses for personnel protection in accelerator tunnels and reaffirmed that neutrons are the dominant component. In addition, comparative studies of shielding materials with different densities have examined the neutron attenuation performance of concrete, soil, and metallic structures in detail [25-29].In recent years, the effects of boron-added materials on shielding performance have gained increasing attention. Sarıyer (2025) demonstrated that ferroboron (Fe_2 B)-based materials are more effective than conventional concrete in reducing neutron doses in high-energy proton accelerators [30]. In particular, a study by Sarıyer (2026) developed a hybrid MC-ML approach for rapid and reliable prediction of secondary neutron dose distributions in high-energy proton facilities [31]. Furthermore, Sarıyer and Yıldırım (2026) proposed a new approach by integrating MC simulations with machine learning techniques for neutron dose prediction in shielding design [32]. Another study by Gökcan and Sarıyer (2026) evaluated shielding performance against secondary neutron radiation using a combination of FLUKA-based MC

simulations and ML methods [33].The effect of material type and composition on secondary radiation fields in proton accelerator shielding has been investigated in numerous studies [25-29]. The effectiveness of concrete in neutron moderation and its success in attenuating low-energy neutrons due to its hydrogen content are well established in the literature [26,34,35]. On the other hand, high atomic number materials such as iron are effective in attenuating high-energy particles but may also increase secondary neutron production, as reported in various studies. This has led to the development of multilayer and hybrid shielding approaches instead of single-material solutions [23,24,36].Studies on multilayer shielding systems have shown that material sequence and the number of layers play a decisive role in dose distribution. In particular, hybrid systems combining high-Z and low-Z materials significantly alter neutron spectra and dose gradients. However, most existing studies focus on systems with a limited number of layers or symmetric geometries. Systematic and comparative investigations of iron-based multilayer shielding systems remain limited. In particular, comprehensive studies directly comparing multilayer iron–concrete shielding configurations in terms of secondary particle production and two-dimensional dose distribution maps are scarce [23,24,36-38]. Nevertheless, iron has strong potential for attenuating high-energy secondary particles due to its high density and atomic number, and its combination with concrete is expected to activate complementary attenuation mechanisms.In this study, the secondary particle field generated by 50 MeV protons interacting with a target material was comparatively investigated under two different multilayer shielding configurations composed of concrete and iron. In the first design, a complex multilayer hybrid structure with multiple iron layers distributed within concrete regions was employed. In the second design, a simplified configuration consisting of a single inner iron layer surrounded by concrete layers was used. This approach allows a systematic evaluation of the effects of layer number, material sequence, and geometric distribution on secondary particle production and transport.Calculations were performed using the FLUKA MC code, and secondary particle production, spatial distributions, and two-dimensional dose distribution maps were obtained for both shielding configurations. The results reveal the effects of different multilayer shielding architectures on the radiation field and provide important physical insights for shielding optimization in medium-energy proton accelerator applications. In this respect, the study aims to fill a significant gap in the literature by systematically analyzing iron–concrete multilayer shielding systems and to contribute to the development of new and optimized shielding design approaches.

2. Material and Methods

2.1 General Approach and Simulation Framework

In this study, secondary particle production in proton accelerators and the transport behavior of these particles within multilayer shielding systems were investigated using MC-based simulation methods. The simulations were performed using the FLUKA MC particle transport code, which is capable of modeling the interactions of medium-energy protons with matter based on detailed physical models. FLUKA is widely used in accelerator physics, radiation protection, and shielding design studies due to its ability to reliably simulate hadronic and electromagnetic interaction processes over a broad energy range and to calculate secondary particle production using statistical methods.Within the scope of this study, secondary particle production and transport resulting from nuclear interactions of 50 MeV protons with a copper target were analyzed in detail. This energy range represents medium-energy proton accelerators, where neutron production—primarily originating from inelastic proton-nucleus interactions and evaporation processes—becomes dominant. Among the secondary particles generated in proton-target interactions, neutrons were considered the primary component governing shielding performance due to their broad energy spectrum and high penetration capability.In the simulations, the DEFAULTS: SHIELDING physics model of FLUKA was employed, and all particle transport processes were statistically tracked within a three-dimensional geometry. To ensure sufficient statistical accuracy, an appropriate number of particle histories was selected, and the reliability of the results was verified by controlling statistical uncertainties.

2.2 Geometrical Model and Boundary Conditions

The simulation geometry was constructed in three dimensions to represent a proton accelerator tunnel. The geometry was defined using FLUKA's combinatorial geometry approach based on rectangular parallelepipeds (RPP) and Boolean operations. The accelerator system and shielding structures were modeled as coordinate-based rectangular prism regions.The accelerator tunnel was modeled as a rectangular volume filled with air, defined within the boundaries of −250 cm to +250 cm in the x-direction, 0 cm to 500 cm in the y-direction, and −500 cm to +500 cm in the z-direction.

The tunnel was positioned within a larger spherical computational domain, where the upper region outside the tunnel was defined as air and the lower region as soil. A blackhole region was implemented at the outer boundary of the geometry to prevent particle reflections.A copper target with approximate dimensions of 5 × 5 × 5 cm³ was defined near the center of the tunnel and designated as the primary source region where proton-nucleus interactions occur. The proton source was placed at the geometric center of this target volume, ensuring that secondary particle production initiates directly within the target. The generated particles then propagate multidirectionally into the surrounding shielding system.Figure 1 presents a schematic configuration of the accelerator tunnel geometry, the multilayer shielding system, and the central copper target. This representation illustrates the relationship between the defined three-dimensional model and the coordinate system used in the simulations, as well as providing a conceptual visualization of secondary particle transport pathways within the shielding structure.

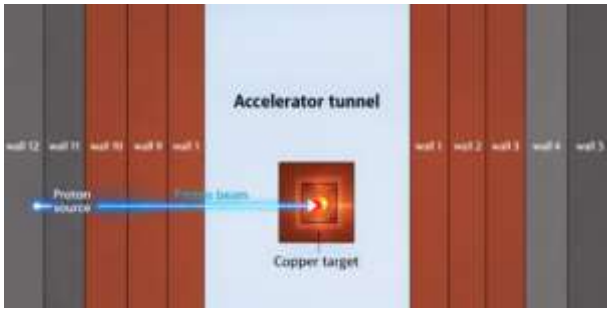

Figure 1. *Cross-sectional schematic of the accelerator tunnel geometry showing the central copper target and the proton source interaction region.*

Two different multilayer shielding designs composed of concrete and iron materials were investigated in this study. In Design 1 (Multilayer Hybrid Shield), the shielding system consists of multiple iron layers positioned near the inner region and along the lateral directions, followed by successive concrete layers. The repeated placement of iron layers at different locations within the shielding structure enhances secondary particle production and scattering processes, resulting in a more complex transport behavior. This configuration provides a multilayered and heterogeneous medium that is effective both in attenuating medium-energy particles and in reshaping the neutron energy spectrum.In Design 2 (Simplified Hybrid Shield), the shielding system consists of a single iron layer located near the inner region, surrounded by concrete layers. This structure, which contains fewer layers, allows the effects of material sequence and layer number to be examined in a more isolated manner.The simulation volume was bounded by two concentric spherical surfaces centered at (0,0,0). The inner and outer radii were defined as 2400 cm and 2500 cm, respectively, and the 100 cm thick region between these surfaces was assigned as a BLACKHOLE material. This approach prevents backscattering of particles leaving the computational domain and ensures well-defined boundary conditions. The overall geometrical configuration and tunnel placement are schematically illustrated in Figure 2.

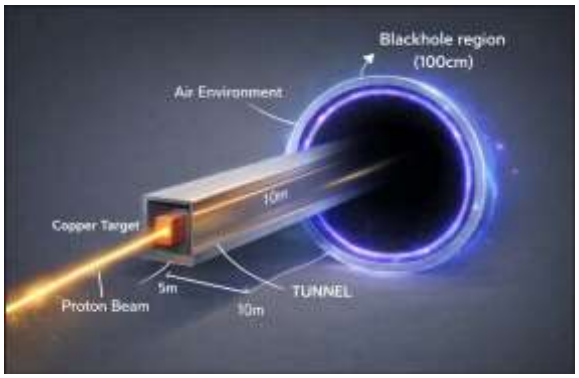

Figure 2. *Schematic representation of the simulation volume defined by concentric spherical boundaries, including the 100 cm thick BLACKHOLE region and the proton accelerator tunnel geometry.*

The accelerator tunnel is surrounded by a multilayer shielding system designed to attenuate the radiation field generated by proton–target interactions. The shielding system consists of rectangular parallelepiped layers arranged sequentially on both sides of the tunnel. These layers are defined as WALL regions in the FLUKA geometry description and form a multilayer wall structure with equal thicknesses along the x-direction. The layers were modeled symmetrically on both sides of the tunnel. This multilayer configuration is intended to provide gradual attenuation of medium-energy neutrons and other secondary particles within the shielding system.In both designs, the shielding system was modeled as a multilayer structure along the tunnel side walls, and an additional concrete floor/shield was defined at the bottom of the tunnel. The concrete floor/shield was specified within the boundaries of $-1500 \leq x \leq 1500$ cm, $-800 \leq y \leq 0$ cm, and $-1000 \leq z \leq 1000$ cm. This structure was included in the model to investigate the attenuation of downward particle transport. Beneath and surrounding the concrete base, a soil region representing the natural ground environment was defined. The tunnel interior and regions outside the shielding system were filled with air.

2.3 Source Definition, Beam Characteristics, and Physical Modeling

The primary particle source was defined as a monoenergetic proton beam with an energy of 50 MeV. The source was positioned at x = 0, y = 100, and z = 0 using the BEAM and BEAMPOS cards in FLUKA, and particles were directed along the +z axis. The direction cosines were defined as $\cos_x = 0$ and $\cos\square = 0$, with the third component set to unity, thereby establishing the transport direction.The system was modeled under an abnormal operating condition corresponding to a point beam loss scenario, and the beam loss was assumed to be 10 W. This corresponds to approximately 6.24×10^{13} protons/s, while for 50 MeV energy, an effective value of 12.480×10^{11} protons/s was considered.The source was modeled as a point source located at the geometric center of the copper target volume. In this way, protons were initiated directly within the target, eliminating entrance surface effects. As a result of proton-nucleus interactions, intranuclear cascade and nuclear evaporation processes occur, producing secondary particles with a broad energy spectrum, particularly neutrons.The simulations were performed using the DEFAULTS SHIELDING physics configuration of FLUKA, including hadronic interactions, electromagnetic processes, and thermal neutron transport.

2.4 Multilayer Shielding Configurations

In this study, two different multilayer shielding designs composed of concrete and iron materials were modeled to investigate the transport behavior of secondary particles generated by 50 MeV proton–target interactions. Both designs were defined using the same geometrical framework, tunnel dimensions, and boundary conditions, with only the material distribution and arrangement of the shielding layers being varied. This approach enables a direct comparison of the effects of material configuration on secondary particle production and spatial dose distribution. The shielding system consists of rectangular layers arranged sequentially along the x-direction on both sides of the accelerator tunnel.

2.4.1 Design 1: Multilayer Iron-Concrete Hybrid Shield Configuration

The first shielding design considered in this study was modeled as a multilayer and symmetric iron–concrete shielding structure surrounding the proton accelerator tunnel. The geometry was defined symmetrically along the x-axis, with shielding layers arranged sequentially in both the +x and −x directions.The accelerator tunnel was defined as a rectangular volume filled with air, bounded within −250 cm to +250 cm in the x-direction, 0 cm to 500 cm in the y-direction, and −500 cm to +500 cm in the z-direction. The first shielding layer surrounding this tunnel volume (Wall 1) extends from −350 cm to +350 cm in the x-direction, 0-1300 cm in the y-direction, and −500 cm to +500 cm in the z-direction, corresponding to an approximate thickness of 100 cm. This layer was defined as iron and represents the primary shielding region where the initial interactions of high-energy particles occur.Outside Wall 1, two additional iron layers were placed in each direction along the x-axis. In the positive x-direction, these layers are defined within the ranges of 350–450 cm and 450–550 cm, while in the negative x-direction they are defined within −450 to −350 cm and −550 to −450 cm. Each of these layers has an approximate thickness of 100 cm and was modeled using iron material. These intermediate iron layers were introduced to enhance the attenuation of medium-energy secondary particles and to provide a buffer region where hadronic interactions continue.Beyond the iron layers, five concrete shielding layers were defined in both positive and negative x-directions. In the positive x-direction, the concrete layers are located at 550–650 cm, 650–750 cm, 750–850 cm, 850–950 cm, and 950–1050 cm. In the negative x-direction, they are defined within −650 to −550 cm, −750 to −650 cm, −850 to −750 cm, −950 to −850 cm, and −1050 to −950 cm. Each concrete layer has a thickness of 100 cm and plays a significant role in neutron moderation and energy loss processes.With this configuration, the total shielding thickness in a single direction from the tunnel center to the outer boundary is approximately 800 cm. The iron layers located in the inner regions contribute to the rapid attenuation of medium-energy particles, while the concrete layers positioned in the outer regions play a dominant role in neutron moderation and dose reduction. Multiple scattering and secondary particle production processes

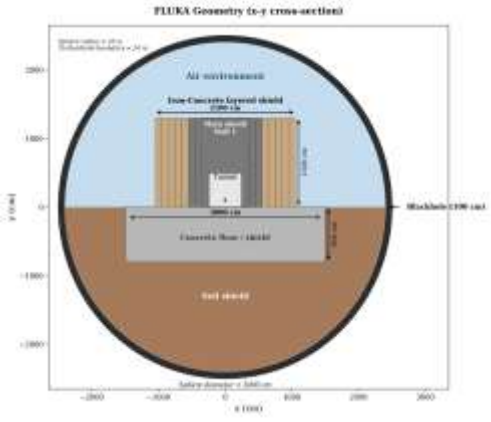

Figure 3. *Schematic cross-sectional (x-y plane) representation of the multilayer shielding geometry used in the FLUKA simulations. The configuration consists of a central accelerator tunnel surrounded by a composite barrier structure including 3-layer iron and 5-layer concrete shielding blocks.*

occurring at the interfaces between different materials lead to the formation of spatially complex and non-linear dose distributions within the system. The geometrical configuration of Design 1 is schematically illustrated in Figure 3.

2.4.2 Design 2: Simplified Multilayer Iron-Concrete Shielding Configuration

The second shielding design used in this study was modeled as a simplified iron–concrete shielding structure with fewer layers and a reduced material complexity surrounding the proton accelerator tunnel. Similar to the first design, the geometry was defined symmetrically along the x-axis, with shielding layers arranged sequentially in both the +x and −x directions.The accelerator tunnel was defined as a rectangular air-filled volume bounded within −250 cm to +250 cm in the x-direction, 0 cm to 500 cm in the y-direction, and −500 cm to +500 cm in the z-direction. The layers surrounding this tunnel volume in both directions extend from −450 cm to +450 cm along the x-axis, 0–500 cm in the y-direction, and −500 cm to +500 cm in the z-direction, corresponding to a total thickness of approximately 200 cm. These layers were defined as iron and modeled as the primary shielding region surrounding the tunnel.Outside this main iron layer, one concrete layer was placed on each side along the x-axis. In the positive x-direction, the concrete layer extends from 450 cm to 850 cm, while in the negative x-direction it is defined between −850 cm and −450 cm. Each of these layers has a thickness of 400 cm and was modeled using concrete material.In addition, a roof shielding component was defined as an additional shielding element in the upper region of the accelerator tunnel. This roof shield extends from −450 cm to +450 cm in the x-direction, 500 cm to 1300 cm in the y-direction, and −500 cm to +500 cm in the z-direction, fully covering the upper part of the tunnel.This integrated shielding structure provides a three-dimensional protection approach that simultaneously restricts particle transport in multiple directions, enabling a more homogeneous and controlled formation of spatial dose distributions. The geometrical configuration of Design 2 is schematically illustrated in Figure 4.

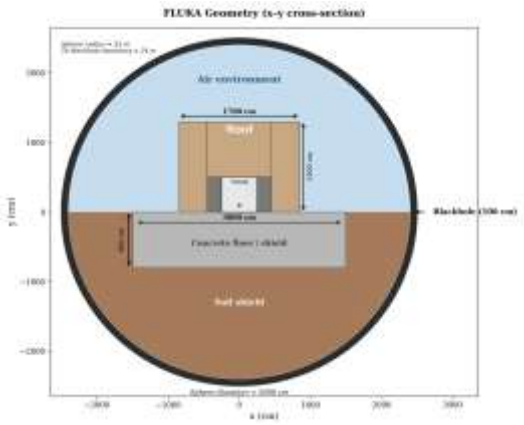

Figure 4. *Schematic cross-sectional (x–y plane) representation of the alternative multilayer shielding geometry used in the FLUKA simulations.*

2.5 Material Composition and Definitions

All materials used in the model were defined in the FLUKA code using the MATERIAL and COMPOUND cards and assigned to the corresponding geometrical regions via the ASSIGNMA card.The concrete material (ρ = 2.34 g cm^{-3}) was modeled using a composition consisting of C, O, Si, Ca, H, and Mg elements. The hydrogen atoms present in concrete contribute to the effective slowing down of fast neutrons through elastic scattering, while heavier elements such as silicon and calcium assist in reducing the neutron energy spectrum via inelastic scattering processes.The iron shielding material (ρ = 7.87 g cm^{-3}) was defined as a homogeneous structure composed of Fe. Owing to its high atomic number and density, iron plays a significant role in reducing the energy of high-energy neutrons through inelastic interactions and intranuclear processes.The soil region (ρ = 1.9 g cm^{-3}) was defined using a composition consisting of O, Si, Al, Fe, Ca, Mg, Na, and K elements, contributing particularly to the additional attenuation of downward neutron flux. The air regions were modeled using a mixture of N, O, and Ar elements with a density of ρ = 0.00120484 g cm^{-3} to ensure the continuity of neutron transport under open environmental conditions.

2.6 Calculation Methodology, Dose Evaluation, and Computational Framework

Secondary particle production, including neutrons, protons, photons, and light nuclear fragments, was evaluated in terms of production yields per primary proton using FLUKA output files. Due to the wide range of obtained values, the analyses were performed on a logarithmic scale.To determine dose distributions and to characterize the spatial structure of the radiation field, a three-dimensional volumetric scoring approach was adopted. In this context, the USRBIN detector available in FLUKA was employed. The scored quantity was the ambient dose equivalent H*(10), and the calculations were carried out using a voxel-based mesh structure. The scoring volume was defined with 340 bins in the x-direction spanning −1700 cm to +1700 cm, 300 bins in the y-direction spanning −1200 cm to +1800 cm, and 190 bins in the z-direction spanning −950 cm to +950 cm. This configuration provided a spatial resolution on the order of approximately 10 cm, enabling

detailed and reliable analysis of dose distributions across the shielding systems.The dose distributions were evaluated along both horizontal and vertical directions, and two-dimensional dose maps were obtained. This approach allowed a comparative assessment of the effects of different shielding designs on the radiation field.Due to the high computational cost of MC simulations, all analyses were performed using a high-performance computing (HPC) infrastructure. The simulations were executed on the TR-Grid cluster system, with 2×10^7 particle histories tracked per cycle, reaching a total of 1×10^8 particle histories. Independent cycles were statistically combined to improve the reliability of the results, and the final dose distributions were obtained accordingly.

3. Results

Secondary particle production resulting from the interaction of 50 MeV protons with a copper target and the transport behavior of these particles within multilayer shielding systems were comparatively investigated for two different shielding configurations in this study. The considered shielding structures were defined as Design 1 (multilayer concrete-iron hybrid shielding) and Design 2 (simplified concrete-iron shielding). The spatial characteristics of the resulting secondary radiation field for each design were evaluated using two-dimensional dose distribution maps.The obtained results indicate that the material type, number of layers, and layer arrangement in the shielding system significantly affect not only the radiation attenuation performance but also the spatial distribution of secondary particles. The total number of secondary particles produced per primary proton was found to be nearly identical for both designs. The total particle production was calculated as 0.1561 and 0.1559 particles per proton for Design 1 and Design 2, respectively. This result suggests that the overall level of nuclear interactions within the system is largely preserved despite the geometrical simplification.In terms of secondary particle types, both designs exhibited a similar distribution. Photons provided the highest contribution in terms of particle number, followed by neutrons, protons, and alpha particles, while the contribution of deuterons was negligible. This finding indicates that the fundamental hadronic interaction processes and secondary particle production mechanisms remain largely unchanged between the two shielding configurations. However, similar particle yields do not imply similar spatial dose distributions. The dose maps clearly demonstrate significant spatial differences between the two designs. This observation highlights that shielding performance is governed not only by the total number of generated secondary particles but also by their transport, scattering, moderation, and attenuation processes within the shielding medium.Within the considered energy range, neutrons emerge as the most critical secondary component from a shielding perspective. This is primarily due to their neutral nature and high penetration capability, which allow them to propagate over large volumes and play a dominant role in shaping the dose field.In Design 1, the sequential and multilayer arrangement of iron and concrete layers introduces a large number of material interfaces within the system. Multiple scattering, energy loss, and secondary particle redistribution processes occurring at these interfaces result in a more complex particle transport behavior. Consequently, the two-dimensional dose distribution maps exhibit more pronounced dose gradients, local irregularities, and a more spatially extended and heterogeneous radiation field.In contrast, Design 2 exhibits a more regular transport behavior due to its reduced number of layers and simplified material configuration. The limited number of interfaces decreases secondary particle scattering and redirection processes, leading to smoother transitions and a more controlled spatial dose field in the dose maps.When both designs are evaluated together, it is observed that the multilayer and heterogeneous Design 1 yields nearly identical total secondary particle production compared to Design 2, yet results in a more complex and spatially extended dose distribution. In contrast, Design 2, despite producing a similar number of secondary particles, organizes the radiation field in a more confined and homogeneous manner. These findings demonstrate that shielding performance is governed not only by particle production but also by geometric arrangement, layer organization, and material interfaces.Overall, material selection, layer thickness, and layer arrangement in multilayer shielding systems play a critical role in shaping the secondary radiation field. In this energy regime, where neutron transport is dominant, shielding optimization is essential not only for reducing the total dose but also for controlling the spatial distribution of the dose field.

3.1 Secondary Particle Production Mechanisms and Evaluation of Relative Contributions

Figures 5 and 6 present the distributions of secondary particles generated by the interaction of 50 MeV protons with a copper target under two different multilayer shielding configurations. The results are expressed in terms of particle contributions per primary proton for each design.

Figures 5(a) and 5(b) present the relative contributions of secondary particle types generated by the interaction of 50 MeV protons with a copper target for Design 1 and Design 2 shielding configurations, respectively. The results indicate that the total secondary particle production is nearly identical for both designs, with values of 0.1561 and 0.1559 particles per primary proton obtained for Design 1 and Design 2, respectively.An analysis of secondary particle types shows that photons provide the highest contribution in both configurations (49.8–49.9%). This behavior reflects the dominant role of gamma emission during the de-excitation of excited nuclei formed in proton–nucleus interactions. Photons are followed by neutrons (~27%), protons (16.8–16.9%), and alpha particles (5.9–6.0%), while the contribution of deuterons remains negligible (~0.3%).The comparative plot shown in Figure 6 further highlights this similarity, where the relative contribution ratios for all particle types nearly overlap between the two designs. The very small differences observed for protons and alpha particles (on the order of ~0.1%) can be attributed to statistical fluctuations or minor variations in secondary interactions during particle transport.These results clearly demonstrate that secondary particle production alone is not a sufficient parameter for evaluating shielding performance. Although both configurations produce similar types and amounts of secondary particles, differences in particle transport, scattering, and attenuation within the shielding medium lead to distinct spatial dose distributions.

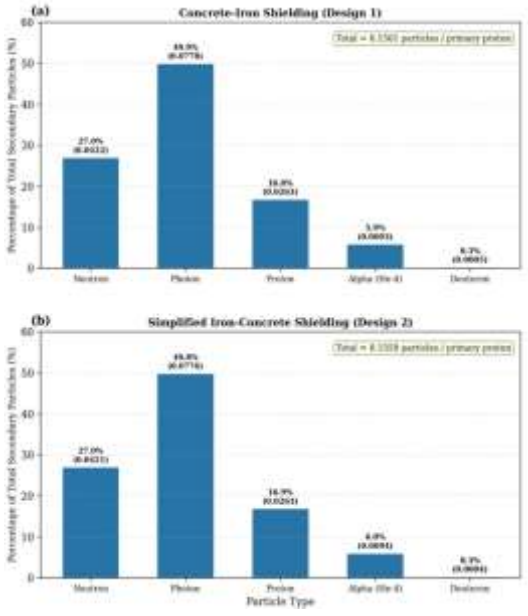

Figure 5. *Relative contributions of secondary particle types produced by the interaction of 50 MeV protons with a copper target: (a) particle percentages and total production per primary proton for Design 1, and (b) for Design 2.*

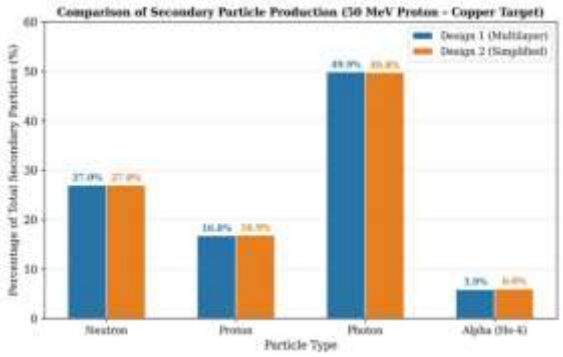

Figure 6. *Comparison of secondary particle production for the 50 MeV proton–copper target interaction: comparative representation of relative contributions by particle type for the Design 1 and Design 2 shielding configurations.*

3.2 Analysis of 2D Spatial Dose Distributions of Secondary Particles in Multilayer Shielding Systems

Figure 7 presents the two-dimensional (2D) dose distribution maps of secondary particles generated by the interaction of 50 MeV protons with a copper target for two different shielding configurations. These maps are calculated based on the ambient dose equivalent H*(10) and provide a detailed representation of the spatial variation of the radiation field within the shielding systems.Figure 8 shows a comparative representation of the dose distributions for the two different shielding designs, where (a) corresponds to Design 1 and (b) to Design 2.An examination of the dose distribution maps presented in Figure 7 on a linear scale reveals that, for both shielding configurations, the maximum dose is concentrated in the source region and gradually decreases with increasing distance from the center. However, in the Design 1 configuration, the dose distribution extends over a larger volume and exhibits a more diffuse pattern, particularly in the upper regions.The logarithmic-scale dose distributions presented in Figure 8 further emphasize the differences, particularly in low-dose regions. In this representation, Design 1 exhibits a wider spatial spread of low-dose levels and a more irregular structure along the shielding–ground interface. In contrast, Design 2 demonstrates a sharper attenuation behavior in low-dose regions, with dose levels decreasing more rapidly.When both figures are considered together, it becomes evident that, although the total secondary particle production is similar for both designs, the shielding geometry plays a decisive role in determining the spatial extent of the dose field. The multilayer configuration (Design 1) produces a more extended and heterogeneous dose distribution, whereas the

simplified configuration (Design 2) provides a more confined and controlled radiation field. These results demonstrate that not only material selection but also geometric arrangement and layer organization are critical parameters in effective shielding design.

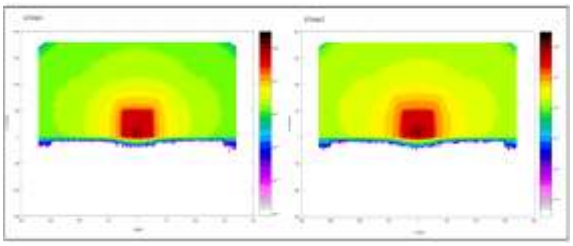

Figure 7. *Two-dimensional (2D) dose distribution maps in the x–y plane of the secondary radiation field generated by the interaction of 50 MeV protons with a copper target. The distributions, calculated in terms of ambient dose equivalent H*(10), are presented for two different shielding configurations: (a) Design 1 and (b) Design 2.*

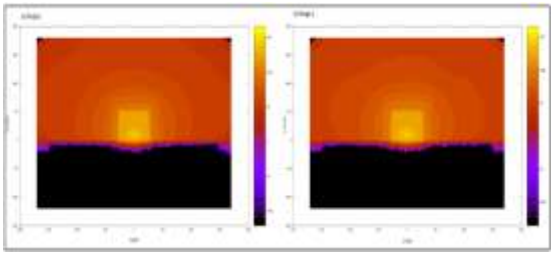

Figure 8. *Comparative representation of ambient dose equivalent H*(10) distributions in the x–y plane for the two shielding configurations: (a) Design 1 and (b) Design 2.*

4. Conclusions

In this study, secondary particle production resulting from the interaction of 50 MeV protons with a copper target and the transport behavior of these particles within multilayer shielding systems were comparatively investigated for two different shielding configurations. The findings obtained using FLUKA Monte Carlo simulations clearly demonstrate that shielding geometry and layer organization play a decisive role in determining the spatial characteristics of the secondary radiation field.The results indicate that the total number of secondary particles produced per primary proton and the relative contributions of particle types are largely similar for both shielding designs. This observation suggests that secondary particle production mechanisms are primarily governed by proton–target interactions and are only marginally affected by the shielding geometry. However, the dose distribution maps reveal significant spatial differences between the two configurations despite similar particle production levels.In the Design 1 configuration, which exhibits a multilayer and heterogeneous structure, the increased number of material interfaces enhances multiple scattering and secondary particle redistribution processes. This leads to a more spatially extended and irregular dose field. In contrast, the Design 2 configuration, characterized by a simpler and less layered structure, produces a comparable number of secondary particles but enables more confined and homogeneous control of the radiation field.These findings demonstrate that shielding performance is governed not only by material selection and total particle production but also by geometric arrangement, layer number, and material interfaces. In radiation fields where neutron transport is dominant, effective shielding design requires not only dose reduction but also precise control of the spatial distribution of radiation.Although photons were found to be numerically dominant in secondary particle production in this study, it is well known that neutron production and its impact become more pronounced at higher energies. Considering the neutral nature and high penetration capability of neutrons, they represent the most critical component from a shielding perspective.It should be noted that the results obtained in this study are valid for a specific energy level (50 MeV), and particle production mechanisms as well as transport behavior may vary at different energy ranges. Therefore, future studies should systematically investigate shielding performance across different proton energy levels in order to provide a more comprehensive understanding of energy-dependent shielding behavior. In addition, the evaluation of alternative shielding designs and material combinations (e.g., boron-doped concretes, ferroboron-based materials, and composite structures) may contribute to the development of more effective and optimized shielding strategies.

Author Statements:

- **Ethical approval:** The conducted research is not related to either human or animal use.
- **Conflict of interest:** The authors declare that they have no known competing financial interests or personal relationships that could have appeared to influence the work reported in this paper
- **Acknowledgement:** The numerical calculations reported in this paper were performed at TUBITAK ULAKBIM, High Performance and Grid Computing Center (TRUBA Resources). **Author contributions:** The authors declare that they have equal right on this paper.
- **Funding information:** The authors declare that there is no funding to be acknowledged.

- **Data availability statement:** The data that support the findings of this study are available on request from the corresponding author. The data are not publicly available due to privacy or ethical restrictions.

References

[1]OECD Nuclear Energy Agency. (2010). Shielding aspects of accelerators, targets and irradiation facilities. *OECD/NEA.*

[2]Titt, U., & Newhauser, W. (2005). Neutron shielding calculations in a proton therapy facility. *Medical Physics*, 32:166-175.

[3]Agosteo, S., Birattari, G., & Silari, M. (2007). Secondary particle production and dose in proton therapy. *Radiation Protection Dosimetry,* 126:397-401.

[4]Vedelago, J., et al. (2024). Monte Carlo study of proton accelerator shielding. *Radiation Physics and Chemistry,* 213:110123.

[5]Agosteo, S., Birattari, G., & Silari, M. (2011). Radiation protection at medical accelerators. *Radiation Protection Dosimetry,* 146:20-25.

[6]Briesmeister, J.F. (Ed.). (2000). MCNP – A general Monte Carlo N-particle transport code. *LA-13709-M, Los Alamos National Laboratory.*

[7]Knoll, G.F. (2010). *Radiation Detection and Measurement.* Wiley.

[8]Shultis, J.K., & Faw, R.E. (2008). *Fundamentals of Nuclear Science and Engineering.* CRC Press.

[9]Turner, J.E. (2007). *Atoms, Radiation, and Radiation Protection.* Wiley.

[10]International Atomic Energy Agency (IAEA). (2006). *Radiation Protection and Shielding. Safety Reports Series No. 47.*

[11]Rockwell, T. (Ed.). (1956). *Reactor Shielding Design Manual.* McGraw-Hill.

[12]Shultis, J.K., & Faw, R.E. (2000). *Radiation Shielding.* American Nuclear Society.

[13]Ferrari, A., Sala, P.R., Fassò, A., & Ranft, J. (2005). FLUKA: A multi-particle transport code. *CERN-2005-010.*

[14]Iwamoto, Y., et al. (2017). Benchmark study of particle and heavy-ion transport code. *Journal of Nuclear Science and Technology,* 54:617-635.

[15]International Atomic Energy Agency (IAEA). (2001). *Compendium of Neutron Spectra. TRS-403.*

[16]Pelowitz, D.B. (Ed.). (2011). MCNPX User's Manual Version 2.7.0. *Los Alamos National Laboratory Report LA-CP-11-00438.*

[17]Agostinelli, S., et al. (2003). GEANT4—a simulation toolkit. *Nuclear Instruments and Methods in Physics Research Section A,* 506:250–303.

[18]Sullivan, A.H. (1992). *A guide to radiation and radioactivity levels near high-energy particle accelerators.* Nuclear Technology Publishing, Ashford.

[19]Liu, J.C., Sullivan, A.H., & Kleck, J.H. (1993). Radiation protection at proton accelerators. *Health Physics,* 65:213–222.

[20]Agosteo, S., Silari, M., & Tosi, G. (2007). Secondary neutron and photon dose in proton therapy facilities. *Radiation Protection Dosimetry,* 126:397-401.

[21]Pelliccioni, M. (2000). Overview of fluence-to-effective dose and fluence-to-ambient dose equivalent conversion coefficients for high energy radiation. *Radiation Protection Dosimetry,* 88:279-297.

[22]Sarıyer, D., & Küçer, R. (2013). Determination of shielding thicknesses for different materials in proton accelerators using an analytical method. *SDU Journal of Science (E-Journal),* 8(1):100-105.

[23]Sarıyer, D. (2017). Effects of different shielding materials on dose distributions for tunnel design in proton accelerators. *Ph.D. thesis, Manisa Celal Bayar University.*

[24]Sarıyer, D., & Küçer, R. (2018). Double-layer neutron shield design as neutron shielding application. *AIP Conference Proceedings,* 1935:180004.

[25]Sarıyer, D., & Küçer, R. (2014). Determination of the shielding thickness required for controlled areas in proton accelerators using the FLUKA Monte Carlo code. *Suleyman Demirel University Journal of Natural and Applied Sciences,* 9:142-149.

[26]Sarıyer, D., & Küçer, R. (2014). Determination of concrete and soil shielding thicknesses for 100–250 MeV proton accelerators using the FLUKA Monte Carlo code. *Suleyman Demirel University Journal of Science,* 9(1):117-124.

[27]Sarıyer, D. (2020). Investigation of neutron attenuation through FeB, Fe_2 B and concrete. *Acta Physica Polonica A,* 137(4):539-542.

[28]Sarıyer, D., Küçer, R., & Küçer, N. (2015). Neutron shielding properties of concrete and ferro-boron. *Acta Physica Polonica A,* 127(2-B):201-202.

[29]Sarıyer, D. (2025). A FLUKA-based study on the effect of boron-enhanced concrete on secondary neutron dose under proton beam loss scenarios. *International Journal of Natural-Applied Sciences and Engineering,* 3(1):113-119.

[30]Sarıyer, D. (2025). FLUKA Monte Carlo assessment of Fe_2 B-based shielding materials for high-energy proton accelerator environments. *International Journal of Computational and Experimental Science and Engineering,* 11:9864-9869.

[31]Sarıyer, D. (2026). Hybrid machine learning–Monte Carlo approach for neutron shielding in high-energy proton facilities. *Journal of Subatomic Particles and Cosmology,* 5:100309.

[32]Sarıyer, D., & Yıldırım, E. (2026). A hybrid Monte Carlo–machine learning framework for high-energy neutron shielding using boron-enhanced concrete. *International Journal of Computational and Experimental Science and Engineering,* 12(1):447–461.

[33]Gökcan, A.O., & Sarıyer, D. (2026). High-energy neutron shielding analysis using curve fitting and machine learning: A Monte Carlo-based study in concrete and ferro-boron configurations. *Annals of Nuclear Energy,* 232:112244.

[34]Barbhuiya, S., Das, B., Norman, P., & Qureshi, T. (2024). A comprehensive review of radiation

shielding concrete: Properties, design, evaluation, and applications. *Structural Concrete*.

[35]Dinter, H., Tesch, K., & Dworak, D. (1996). Studies on the neutron field behind shielding of proton accelerators: Part I – Concrete shielding. *Nuclear Instruments and Methods in Physics Research Section A*, 368:265-272.

[36]Sarıyer, D., Küçer, R., & Küçer, N. (2015). Determination by FLUKA Monte Carlo code of shielding thicknesses of iron in proton accelerators. *Balkan Physics Letters*, 23:37-42.

[37]Yani, S., et al. (2026). Optimization of proton radiation shielding using multilayer concrete–iron–polyethylene barriers: A PHITS Monte Carlo study. *Radiation Physics and Chemistry*, 240:113422.

[38]Aliyah, F. (2024). Multi-layer radiation shielding design for compact proton therapy system using Monte Carlo simulation. *Master's thesis, Universiti Sains Malaysia.*